

## Article

# Stable Nickel-Based Metal–Organic Framework Containing Thiophene/Diimidazole Units for Effective Near-Infrared Photothermal Conversion

Xiangran Pei <sup>1</sup>, Lilong Dang <sup>2</sup>, Tingting Zhang <sup>2</sup>, Tian Chen <sup>2</sup>, Fuxuan Ren <sup>2</sup> and Shuiren Liu <sup>1,\*</sup>

<sup>1</sup> School of Materials Science and Engineering, Zhengzhou University, Zhengzhou 450001, China; pxf15137380173@163.com

<sup>2</sup> Henan Province Function-Oriented Porous Materials Key Laboratory, College of Chemistry and Chemical Engineering, Luoyang Normal University, Luoyang 471934, China; danglilong8@163.com (L.D.); zhangtingting131@126.com (T.Z.); ctian2022@163.com (T.C.); 17772114171@163.com (F.R.)

\* Correspondence: lsrzzdx@zzu.edu.cn

**Abstract:** Herein, a new Ni-based metal–organic framework (MOF, **1**) bearing highly structural stability is synthesized by the reaction of utilizing a rigid and functionalized linker, 2,6-bis(pyridin-4-yl)-1,7-dihydrobenzo[1,2-d:4,5-d']diimidazole (**BBI4PY**), in combination with Ni(NO<sub>3</sub>)<sub>2</sub>·6H<sub>2</sub>O and dibenzo[b,d]thiophene-3,7-dicarboxylic acid 5,5-dioxide (**L1**) under solvothermal conditions. The crystal structure of complex **1** is determined by single-crystal X-ray diffraction and is demonstrated to be a two-dimensional layered structure. In addition, PXRD, IR, TGA and UV/Vis-NIR spectra are also tested carefully to explore the solid structure of this complex. Remarkably, although no significant accumulation effect could be observed between the two-dimensional layers, a stacking interaction between DMF solvent molecules and ligand **L1** could be found, which might promote non-radiative transitions and trigger obvious near-infrared photothermal conversion. Under 660 nm laser (0.6 W cm<sup>−2</sup>) illumination, the temperature of complex **1** increased rapidly from room temperature to 45.2 °C, with good thermal stability and cycle durability. Its photothermal conversion efficiency could reach 10.75%. This work provides an efficient way for assessing the promise of materials in the field of photothermal therapy.

**Keywords:** metal–organic framework; near-infrared photothermal conversion; crystal structure; accumulation effect



**Citation:** Pei, X.; Dang, L.; Zhang, T.; Chen, T.; Ren, F.; Liu, S. Stable Nickel-Based Metal–Organic Framework Containing Thiophene/Diimidazole Units for Effective Near-Infrared Photothermal Conversion. *Catalysts* **2022**, *12*, 777. <https://doi.org/10.3390/catal12070777>

Academic Editor: Gang Li

Received: 17 June 2022

Accepted: 9 July 2022

Published: 13 July 2022

**Publisher's Note:** MDPI stays neutral with regard to jurisdictional claims in published maps and institutional affiliations.



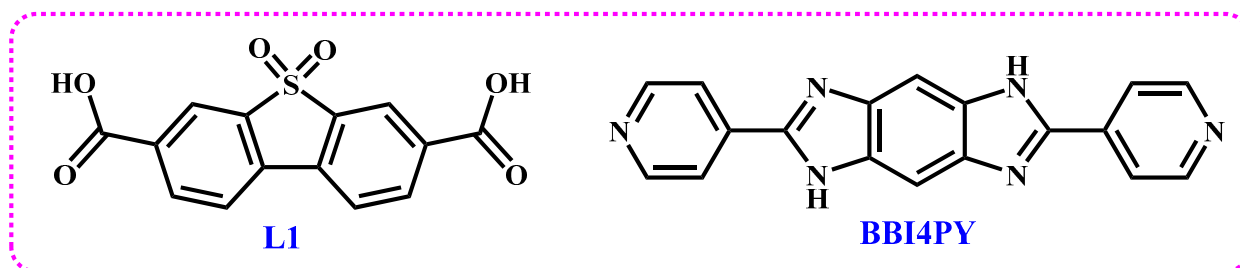
**Copyright:** © 2022 by the authors. Licensee MDPI, Basel, Switzerland. This article is an open access article distributed under the terms and conditions of the Creative Commons Attribution (CC BY) license (<https://creativecommons.org/licenses/by/4.0/>).

## 1. Introduction

Photothermal therapy has great potential for cancer therapy due to the effective and highly selective killing of diseased lesions under the irradiation of light, preferably near-infrared (NIR) light [1–3]. The photothermal agents (PTAs) for converting NIR light to heat are either purely inorganic materials or purely organic materials exemplified by conjugated polymers and molecular dyes [4–7]. However, the disadvantages of the poor photostability and biodegradation of these materials hinder their further application [8–10]. As a new type of crystalline porous inorganic–organic hybrid material, metal–organic frameworks (MOFs) have aroused widespread concern among scientists due to their large specific surface area, highly tunable structures, modular porosity, and structural stability [11–17]. Therefore, various MOF structures, such as MOF-5, MOF-74, ZIF-8, and UTSA-74, have been constructed successfully through various methods; their properties, such as gas adsorption, catalysis, sensors, photoelectric performance, and photothermal effect, have also been explored [18–25]. Several hundred articles about the performance exploration of MOF structures have been reported successfully [26–30]. These studies have also prompted more chemists to design and synthesize additional MOFs with better structures and performance, which will drive the rapid development of and offer a great leap-forward for MOF materials.

In the process of designing functionalized MOF structures bearing photothermal effects, the selection of both metal ions and organic ligands is extremely important. The utilization of metal ions and ligand linkers plays a vital role in the structural construction and performance implementation of MOF structures. For example, Chen reported a ruthenium metal–organic framework; after TCNQ loading, the complex exhibited an enhanced photothermal property with a photothermal conversion efficiency of 29.1% [31]. In addition, various MOF materials bearing near-infrared photothermal conversion performance have been reported [32–36]. For example, a group of researchers synthesized a new Zn-MOF containing an electron donor, tetrathiafulvalene (TTF), and an electron acceptor, naphthalene diimide. Interestingly, the material exhibited wide absorption peaks in the near-infrared region and displayed efficient near-infrared photothermal conversion performance (from room temperature to 250 °C) under 808 nm laser ( $0.4 \text{ W cm}^{-2}$ ) illumination [37]. From previous reports, it can be found that the  $\pi$ - $\pi$  stacking interaction plays an important role in structural generation and photothermal triggering. Thus, the selection of appropriate ligand components to construct an effective stacking interaction is critical for the resulting photothermal effect.

Based on this, a new pillar ligand, 2,6-bis(pyridin-4-yl)-1,7-dihydrobenzo[1,2-d:4,5-d']-diimidazole (**BBI4PY**) with a benz-bis(imidazole) moiety, is selected. Moreover, this new linker has multiple hydrogen bonding and Lewis basic interaction sites, as shown in Scheme 1. Importantly, **BBI4PY** has an obvious conjugate center, which could cause an effective stacking interaction. The choice of this ligand is of great significance for the synthesis of the MOF. Herein, through the solvothermal method based on two organic ligands, 2,6-bis(pyridin-4-yl)-1,7-dihydrobenzo[1,2-d:4,5-d']diimidazole (**BBI4PY**) and dibenzo[b,d]thiophene-3,7-dicarboxylic acid 5,5-dioxide (**L1**), a new Ni-based complex is obtained and its synthesis and crystal structure are reported. Its near-infrared photothermal conversion properties are investigated in detail.



**Scheme 1.** Chemical structures of **L1** and **BBI4PY** in this work.

## 2. Results

### 2.1. The Structure of Complex 1

The crystal structure was demonstrated by single-crystal X-ray diffraction analysis, reflecting that complex **1** crystallized in the triclinic  $P-1$  space group (Table 1). Observing the single-crystal structure, the asymmetric unit contained one crystallography-independent Ni (II) metal center, 0.5 ligand **L1**, 0.5 ligand **BBI4PY**, and two coordinated water molecules (Figure 1a). The nickel cations were coordinated by six atoms, including two carboxyl oxygen atoms of  $\text{L1}^{2-}$  ligands, two pyridine nitrogen atoms from the neutral **BBI4PY** ligand, and two oxygen atoms from two  $\text{H}_2\text{O}$  molecules, respectively. In addition, each  $\text{L1}^{2-}$  ligand could achieve coordination with two nickel cations and two carboxyl oxygen atoms. Each **BBI4PY** ligand connected to two nickel cations, showing a bidentate coordination mode. Finally, a series of rectangular windows ( $19.18 \times 15.32 \text{ \AA}^2$ ) were formed from four nickel cations, two **BBI4PY** ligands, and two  $\text{L1}^{2-}$  ligands (Figure 1b,c). These rectangular windows resulted in the formation of a two-dimensional layered structure. The Ni–O bond lengths were 2.082(5), 2.068(5), 2.083(4), and 1.987(5) Å. At the same time, the lengths of the two Ni–N bonds were 2.109(5) and 2.124(5) Å (Table 2, Figure 1d). In addition, the separation between the two-dimensional layered structures was 7.5 Å, which was

long enough that no interactions between the two layered structures could be detected. However, obvious  $\pi$ - $\pi$  stacking interactions between free DMF molecules and ligands **L1** or **BBI4PY** were found, the distances between which were 3.42 and 3.56 Å, respectively. The stacking interactions might have caused an effective photothermal effect, and the loss and addition of DMF solvent molecules might have led to the disappearance and reappearance of a photothermal effect.

**Table 1.** Crystallographic data and experimental details for complex **1**.

| Complex   | <b>1</b>  |
|---|---|
| Empirical formula   | $C_{76}H_{72}N_{16}Ni_2O_{20}S_2$   |
| Formula weight  | 1711.03   |
| Temperature/K   | 293(2)  |
| Crystal system  | triclinic   |
| Space group   | <i>P</i> -1   |
| <i>a</i> /Å   | 11.6770(5)  |
| <i>b</i> /Å   | 18.4276(15)   |
| <i>c</i> /Å   | 21.3747(11)   |
| Volume/Å <sup>3</sup>   | 4144.5(5)   |
| <i>Z</i>  | 2   |
| $\rho_{\text{calc}}/\text{g cm}^{-3}$                         | 1.371   |
| $\mu/\text{mm}^{-1}$  | 0.583   |
| <i>F</i> (000)/ <i>e</i>                                      | 1776.0  |
| 2 $\theta$ range for data collection/°                        | 6.708 to 50.052   |
| Reflections collected   | 27223   |
| Independent reflections                                       | 14551 [ <i>R</i> <sub>int</sub> = 0.0757, <i>R</i> <sub>sigma</sub> = 0.1491] |
| Data/restraints/parameters                                    | 14551/12/980  |
| Goodness-of-fit on <i>F</i> <sup>2</sup>                      | 1.002   |
| $\Delta\rho_{\text{fin}}$ (max/min), <i>e</i> Å <sup>-3</sup> | 1.27/−0.63  |
| Final <i>R</i> indexes [ <i>I</i> ≥ 2 $\sigma$ ( <i>I</i> )]  | <i>R</i> <sub>1</sub> = 0.0905, <i>wR</i> <sub>2</sub> = 0.1580               |
| Final <i>R</i> indexes [all data]                             | <i>R</i> <sub>1</sub> = 0.1581, <i>wR</i> <sub>2</sub> = 0.1893               |

$$R = [\sum ||F_0| - |F_c|| / \sum |F_0|], R_W = \sum_W [|F_0|^2 - |F_c|^2|^2 / \sum_W (|F_w|^2)^2]^{1/2}.$$

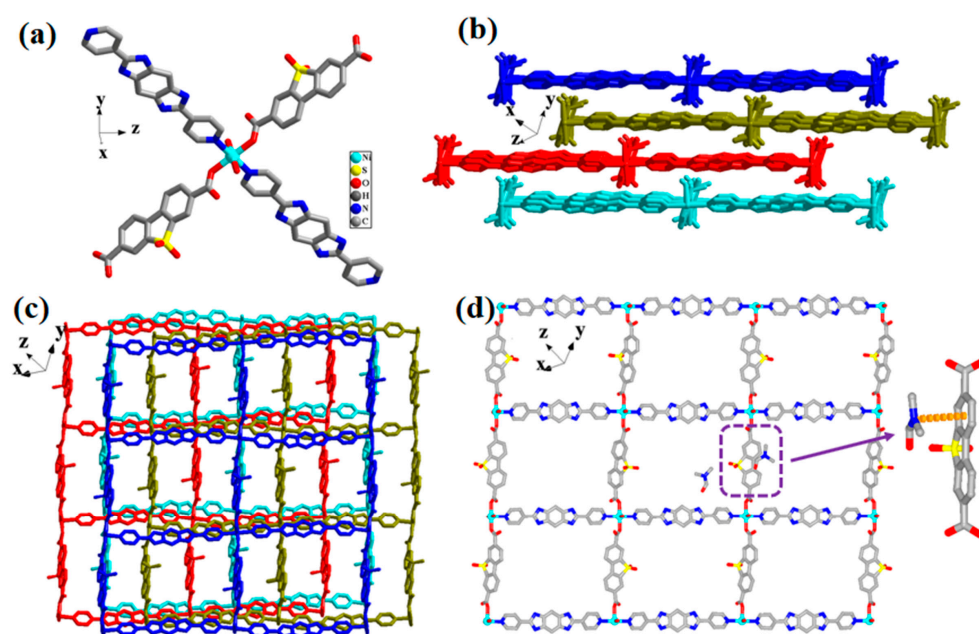


**Figure 1.** (a) Single-crystal X-ray structure of complex **1**. Representation of the Ni(II) coordination environments and ligands' coordination modes in complex **1**. (b) Side view of the stacking framework of complex **1**. (c) View of the stacking framework of complex **1**. (d) View of the 2D framework of complex **1**; insert shows the  $\pi$ - $\pi$  stacking interactions between the DMF molecule and **L1** ligand.

**Table 2.** Selected bond lengths (Å) for complex 1.

|     |                 |          |     |                  |          |
|-----|-----------------|----------|-----|------------------|----------|
| Ni1 | O1 <sup>1</sup> | 2.082(5) | Ni1 | O10 <sup>3</sup> | 2.083(4) |
| Ni1 | O4 <sup>2</sup> | 2.068(5) | Ni1 | O16 <sup>4</sup> | 1.987(5) |
| Ni1 | N8              | 2.124(5) |     |                  |          |
| Ni1 | N9              | 2.109(5) |     |                  |          |

<sup>1</sup> 2-x,2-y,1-z; <sup>2</sup> 1/2+x,7/4-y,5/4-z; <sup>3</sup> 7/4-x,1/2+y,5/4-z; <sup>4</sup> 9/4-x,7/4-y,-1/2+z.

## 2.2. The PXRD and TGA Exploration of Complex 1

To determine the phase purity of synthesized powder complex 1, PXRD measurements were performed carefully. The simulated and experimental PXRD patterns of complex 1 (the latter obtained at room temperature) are shown in Figure 2a. All main diffractive peaks of the powder sample were nearly consistent with the simulated pattern produced from the single-crystal diffraction data, reflecting the good phase purity of the solid-state complex. Moreover, the discrepancy in reflection intensities between the simulated and experimental patterns might be attributed to variations in the preferred orientation of the solid samples. Both the shift between two-dimensional layered structures, due to weak interaction, and the loss of solvent molecules might result in the discrepancy between  $Y_{\text{experimental}}$  and  $Y_{\text{simulate}}$ . Nevertheless, the good match between the main peaks ( $X = 6.9, 8.3, 11.6, 14.5, 21.0$  and  $21.7$ ) proved the stability of the major structure.

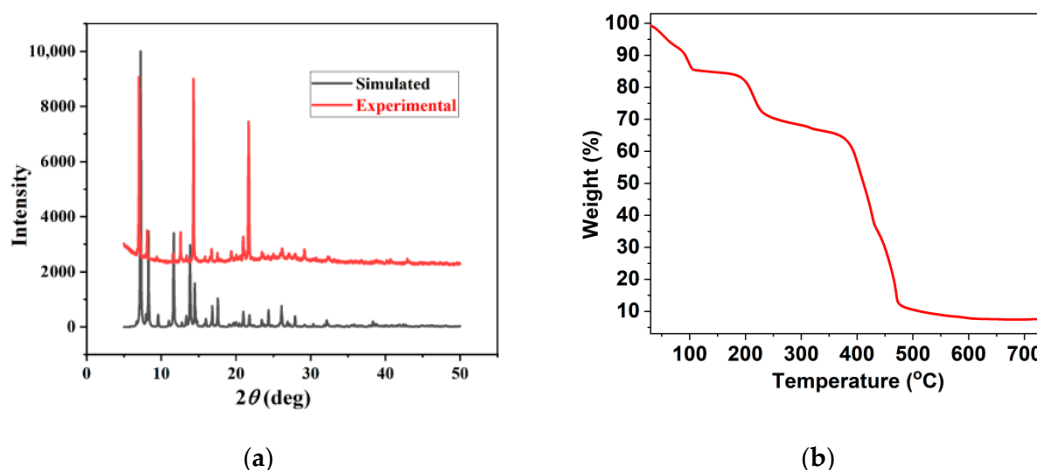


**Figure 2.** (a) PXRD patterns of simulated (black) and the as-synthesized samples (red) of complex 1. (b) Thermogravimetric analysis curve of complex 1. Weight losses were 15.09% for complex 1 in the range of 0–100 °C, which corresponded to the loss of 2.0 free water and DMF molecules (calcd 6.12% for complex 1).

The TG analysis curve of complex 1 is displayed in Figure 2b; the weight loss was 15.09% for complex 1 in the range of 0–100 °C, which corresponded to the loss of 2.0 free water and DMF molecules (calcd 6.12% for complex 1). From 100 to 180 °C, no losses were observed. Then, a weight loss of 10.22% was observed in the range of 100–288 °C, corresponding to the loss of two coordinated water molecules (calcd 10.40% for complex 1). After that, the successive losses from 258 to 500 °C corresponded to the collapse of the skeleton and the decomposition of the organic ligand.

## 2.3. The IR and UV/Vis-NIR Spectra of Complex 1

In addition, the IR spectrum of complex 1, **BBI4PY**, and **L1** are clearly shown in Figure 3. The IR spectrum of complex 1 exhibited a strong band at  $1174 \text{ cm}^{-1}$ , owing to the S=O stretching vibrations, similar to the peak position in the infrared spectrum of **L1**. Strong absorptions at  $1663 \text{ cm}^{-1}$  and  $1248 \text{ cm}^{-1}$  occurred due to the stretching of the C=O and C-O bonds from the carboxylate group of **L1**<sup>2-</sup>, and they all moved to lower wave

numbers in different degrees, as compared to **L1**, possibly due to the coordination of the metal center and the  $\pi$ - $\pi$  stacking interactions. The C-H deformation vibration absorption peaks on the pyridine group were  $1451\text{ cm}^{-1}$ . Furthermore, the characteristic absorption peak of pyridine in the IR spectrum of **BBI4PY** was  $1440\text{ cm}^{-1}$ . Moreover, the analysis of the IR spectrum also showed strong bands at  $1615\text{ cm}^{-1}$  and  $3175\text{ cm}^{-1}$ , attributed to the stretching vibration of the C=N and N-H bonds of the imidazole group. We can unambiguously see that the strong peaks at  $1618\text{ cm}^{-1}$  and  $3373\text{ cm}^{-1}$  are assigned to the C=N and N-H bonds of the imidazole group on the IR spectrum of **BBI4PY** [38–44].

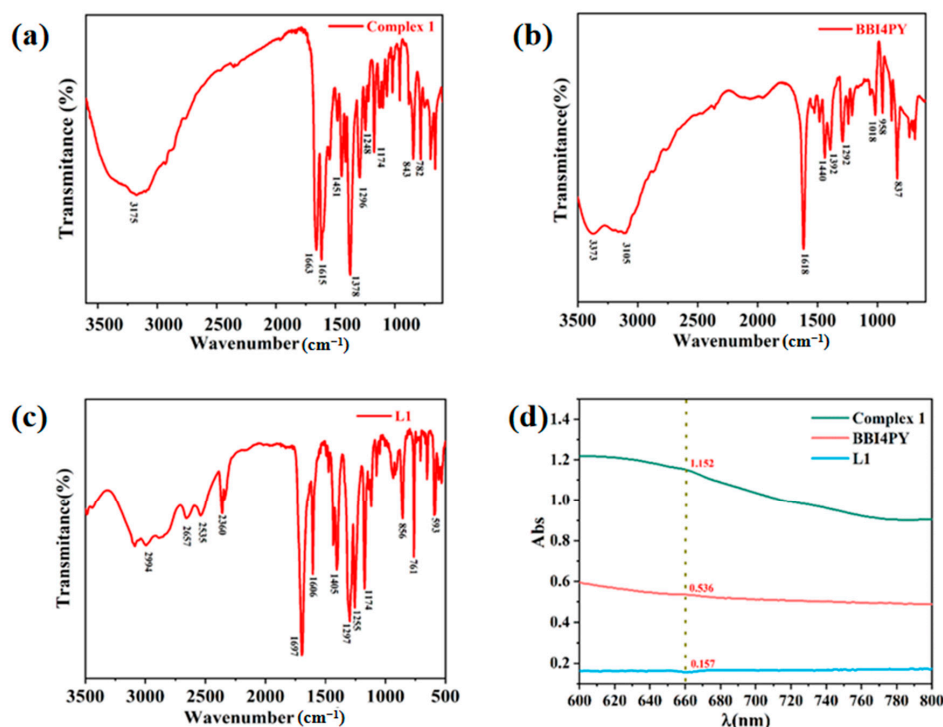


**Figure 3.** (a) The IR spectrum of complex **1**. (b) The IR spectrum of **BBI4PY**. (c) The IR spectrum of **L1**. (d) The absorption of complex **1** in the near-infrared region of the topology at 660 nm.

Moreover, the solid-state UV/Vis-NIR spectra of ligands **L1**, **BBI4PY**, and complex **1** were studied at room temperature. As shown in Figure 3b, there was a broad absorption peak from 600 to 800 nm for complex **1** (Abs: 1.152 at 660 nm), displaying strong absorption in the NIR region. This illustrates the existence of strong stacking interactions in complex **1**, which is consistent with the analysis of the crystal structure. However, for the free ligands **L1** and **BBI4PY**, the adsorption peaks were very weak and the Abs values were 0.536 and 0.157 at 660 nm.

#### 2.4. The Near-Infrared Photothermal Conversion Studies

Previous reports have displayed that  $\pi$ - $\pi$  stacking interactions could induce active nonradiative pathways and the inhibition of the radiative transition process, causing photothermal (PT) conversion [45–49]. Meanwhile, based on the strong absorption of complex **1** in the NIR region, the dark color in the solid state (Figure 4a), and the TGA tests of crystal **1**, it has already been demonstrated that the structural stability of complex **1** could be maintained up to  $200\text{ }^{\circ}\text{C}$ . Therefore, this tells us that the temperature change from the photothermal effect could not cause structural changes (Figure 2b). Therefore, the near-infrared photothermal conversion properties of complex **1** were explored in detail under the infrared light irradiation of 660 nm. As a comparison, the near-infrared photothermal conversion experiments of the two ligands, **L1** and **BBI4PY**, were carried out under the same conditions.

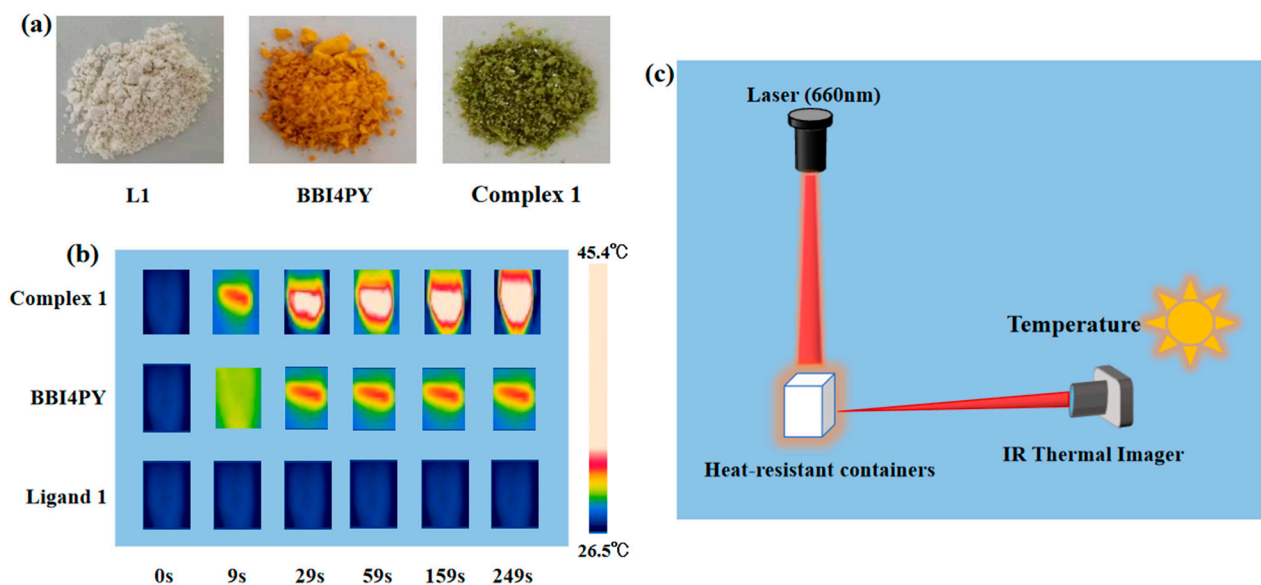


**Figure 4.** (a) The different colors of complex **1**, ligands **L1**, and **BBI4PY**. (b) Photothermal conversion images of complex **1**, ligands **L1**, and **BBI4PY**. (c) Diagram of photothermal conversion measurement.

Therefore, the crystalline complex **1** was irradiated under  $0.6 \text{ W/cm}^2$  laser irradiation at 660 nm in a solid state. The temperature change in crystalline complex **1** reached  $19.1 \text{ }^\circ\text{C}$  (from  $26.3$  to  $45.4 \text{ }^\circ\text{C}$ ) (Figure 4b). This is a viable temperature change. When the laser irradiation of 660 nm was removed, a rapid cooling process was observed clearly by the infrared imaging camera. Based on the reduced temperature data, the near-infrared photothermal efficiency of complex **1** was calculated to be 10.75%, according to the calculation method described below (Equations (1)–(4)), showing good near-infrared photothermal performance of this Ni–MOF, **1**. Meanwhile, the temperature changes of ligands **L1** and **BBI4PY** under laser irradiation at 660 nm for 3 h were also tested. The results showed that although the temperature change of **L1** was very weak and could be ignored, the temperature increase in ligand **BBI4PY** was  $5.3 \text{ }^\circ\text{C}$  (from  $22.0$  to  $27.3 \text{ }^\circ\text{C}$ ), possibly due to the formation of self-accumulation between two **BBI4PY** ligands (Figure 5a). In addition, the cycle performance of photothermal efficiency for complex **1** was explored by continuous  $0.6 \text{ W/cm}^2$  laser irradiation at 660 nm four times, as well as the addition of DMF solvents (Figure 5b). The temperature change in solid crystalline **1** could still reach  $45.2 \text{ }^\circ\text{C}$  every time, clearly reflecting high stability and photothermal efficiency in the cycle performance. The absence of fluorescence in the crystal indicates that the photothermal conversion effect was realized by non-radiative transition. It also reflects that stacking interactions play an important role in the stability and photothermal properties of crystal **1**. According to the above experimental data, we can infer a rule of experience: the photothermal conversion efficiency is relevant to  $\pi$ - $\pi$  stacking interactions.

$$\eta = hS (\Delta T_{\text{sample}} - \Delta T_{\text{solvent}}) / I(1 - 10^{-A}) \quad (1)$$

$$hS = \sum mC_p / \tau_s \quad (2)$$

$$\tau_s = -t / \ln \theta \quad (3)$$

$$\theta = (T_{\text{amb}} - T) / (T_{\text{amb}} - T_{\text{max}}) \quad (4)$$

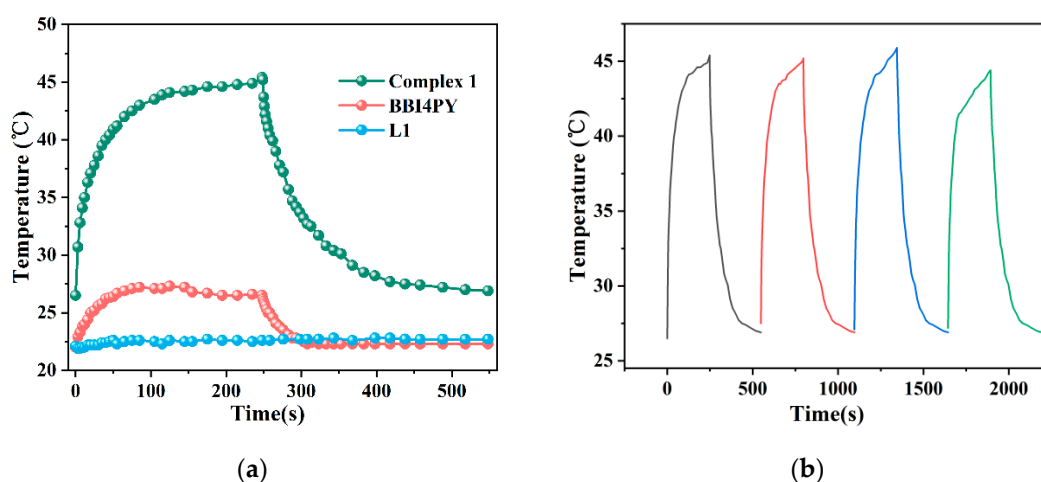


**Figure 5.** (a) Photothermal conversion curve of complex 1. (b) Photothermal conversion cycle experiments: solid state of complex 1.

In Equations (1)–(4) above,  $h$  is the heat transfer coefficient,  $S$  is the surface area of the container,  $\tau_s$  is the sample system time constant,  $m$  is the mass of the products,  $C_p$  is the specific heat capacity of the solvent, and the value of  $\tau_s$  was obtained from the fitting linear of these solutions (Figure 6).

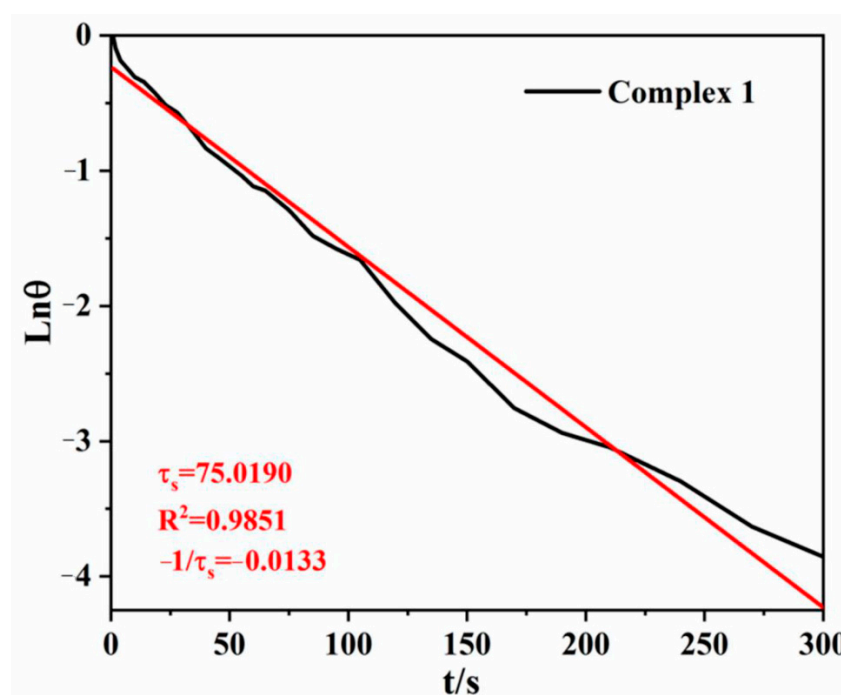


**Figure 6.** Fitting linear of  $\ln\theta$ – $t$  in the solid state of complex 1 under the laser irradiation of  $0.6 \text{ W/cm}^2$ .

### 3. Experiment

#### 3.1. Materials and Methods

The selected reagents were analytic-grade and acquired through commercial sources. They were utilized without further purification. Elemental analyses for C and H were carried out on a Perkin-Elmer 240 elemental analyzer. The FT-IR spectra were tested from KBr pellets in a particular range from  $4000$  to  $400 \text{ cm}^{-1}$  on a Bruker VECTOR 22 spectrometer. The UV/Vis-NIR spectra were tested in a particular range from  $600$  to  $800 \text{ nm}$  on a UV-3100 spectrophotometer. Thermal analysis measurements were executed on an

SDT 2960 thermal analyzer from 25 °C to 800 °C, based on a heating rate of 20 K min<sup>-1</sup> under nitrogen flow. Powder X-ray diffraction (PXRD) data were collected smoothly on a Rigaku D/Max-2500PC diffractometer with Cu K $\alpha$  radiation ( $\lambda = 1.5406 \text{ \AA}$ ) over the 2 $\theta$  range of 5–50° with a scan speed of 5°/min at 25 °C.

Solid-state UV-Vis-NIR spectra were measured on a UV-3100 spectrophotometer. BaSO<sub>4</sub> was used as the reference. Spectra are reported as the Kubelka–Munk transform, where  $F(R) = (1 - R)^2 / 2R$  ( $R$  is the diffuse reflectance of the sample as compared to BaSO<sub>4</sub>).

The single-crystal X-ray diffraction analysis of complex **1** was carried out on a Rigaku Saturn 724 CCD diffractometer (Mo-K $\alpha$ ,  $\lambda = 0.71073 \text{ \AA}$ ) at room temperature. The structure was solved by Direct Methods with SHELXS-97 and refined by the full-matrix least-squares method on F2 with anisotropic displacement parameters for all non-H atoms (SHELXL-97). An empirical absorption correction was applied by the SADABS program [50,51]. The hydrogen atoms were assigned with common isotropic displacement factors and included in the final refinement by the use of geometrical restraints. The crystallographic data and selected bond lengths and angles for complex **1** are listed in Tables 1 and 2. Crystallographic data for the structural analysis have been deposited with the Cambridge Crystallographic Data Center, and CCDC No. for compound **1** contains the supplementary crystallographic data for this paper. These data can be obtained free of charge from The Cambridge Crystallographic Data Centre via <http://www.ccdc.cam.ac.uk/Community/Requestastructure> (accessed on 16 June 2022).

### 3.2. Synthesis of Complex 1

A mixture of Ni(NO<sub>3</sub>)<sub>2</sub>·6H<sub>2</sub>O (0.2 mmol, 0.058 g), 2,6-bis(pyridin-4-yl)-1,7-dihydrobenzo[1,2-d:4,5-d']diimidazole (**BBI4PY**) (0.2 mmol, 0.0624 g), dibenzo[b, d]thiophene-3,7-dicarboxylic acid 5,5-dioxide (**L1**) (0.2 mmol, 0.061 g) and 4 mL of DMF and 2 mL of H<sub>2</sub>O was stirred for 10 min. The mixture was then transferred and sealed into a Teflon reactor (23 mL) and heated at 115 °C for 48 h. After that, the mixture was cooled to room temperature. Blue block crystals of complex **1** were washed by ethanol (3 × 10 mL) and dried in air at room temperature (yield: 65% based on Ni). Anal. Calc. (%) for C<sub>76</sub>H<sub>72</sub>N<sub>16</sub>Ni<sub>2</sub>O<sub>20</sub>S<sub>2</sub>: C 53.35, H 4.24, N 13.10; found (%): C 53.31, H 4.26, N 13.12. IR (KBr, cm<sup>-1</sup>): 3175.10(w), 1663.20(w), 1615.60(s), 1451.44(s), 1375.92(m), 1296.31(m), 1174.01(m), 1019.70(w), 963.06(w), 840.77(s), 780.33(s), 699.59(s), 599.85(s), 578.11(s)

### 3.3. X-ray Crystallography

Single-crystal X-ray diffraction data for complex **1** were acquired at 298 K on an Oxford Diffraction SuperNova area-detector diffractometer by utilizing mirror optics monochromated MoK  $\alpha$  radiation ( $\lambda = 0.71073 \text{ \AA}$ ). CrysAlisPro [50] was utilized for the crystal data collection, general data reduction, and further empirical absorption correction. The crystal structure of complex **1** was solved by SHELXS-2014 and least-squares refined with SHELXL-2014 [51]. The crystal refinement parameters are provided in Table 1. A solvent mask was calculated and 188 electrons were found in a volume of 1026 Å<sup>3</sup> in 1 void per unit cell. This is consistent with the presence of 2[C<sub>3</sub>H<sub>7</sub>NO] per asymmetric unit, which accounts for 160 electrons per unit cell.

## 4. Conclusions

In summary, we synthesized a new Ni-based MOF complex by a solvothermal method based on a decarboxylic acid ligand and a bidentate pyridine ligand. Single-crystal X-ray diffraction analysis determined the compound to be a two-dimensional layered structure. A series of structural characterization from PXRD, IR, TGA and UV-vis-NIR spectra showed good structural stability and a wide range of near infrared absorption. In addition, obvious  $\pi$ - $\pi$  stacking interactions could be found, which promoted non-radiative transitions and triggered the effective photothermal conversion effect. The near-infrared photothermal exploration showed a temperature variation of 19.1 °C and the near-infrared photothermal efficiency reached 10.75%, demonstrating good near-infrared photothermal

performance. This research encourages us to synthesize and explore more photothermal conversion materials.

**Author Contributions:** X.P. and L.D., synthesis of the title complex, formal analysis, IR-related experiment; X.P., writing—review and editing; T.Z. and T.C., formal analysis and photo-thermal exploration experiment; F.R., UV/Vis-NIR absorption spectra experiment; S.L.: supervision, writing—review and editing. All authors have read and agreed to the published version of the manuscript.

**Funding:** This work was supported by the National Natural Science Foundation of China (Grant Nos. 52003253 and 22101108), Natural Science Foundation of Henan Province (No. 212300410209), and the Shanghai Science and Technology Committee (19DZ2270100).

**Conflicts of Interest:** The authors declare no conflict of interest.

## References

1. Lyu, Y.; Fang, Y.; Miao, Q.Q.; Zhen, X.; Ding, D.; Pu, K.Y. Intraparticle molecular orbital engineering of semiconducting polymer nanoparticles as amplified theranostics for in vivo photoacoustic imaging and photothermal therapy. *ACS Nano* **2016**, *10*, 4472–4481. [[CrossRef](#)]
2. Pu, K.; Shuhendler, A.J.; Jokerst, J.V.; Mei, J.G.; Gambhir, S.S.; Bao, Z.N.; Rao, J.H. Semiconducting polymer nanoparticles as photoacoustic molecular imaging probes in living mice. *Nat. Nano* **2014**, *9*, 233–239. [[CrossRef](#)]
3. Chen, Q.; Liang, C.; Sun, X.Q.; Chen, J.W.; Yang, Z.J.; Zhao, H.; Feng, L.Z.; Liu, Z. H<sub>2</sub>O<sub>2</sub>-responsive liposomal nanoprobe for photoacoustic inflammation imaging and tumor theranostics via in vivo chromogenic assay. *Proc. Natl. Acad. Sci. USA* **2017**, *114*, 5343–5348. [[CrossRef](#)]
4. Lovell, J.F.; Jin, C.S.; Huynh, E.; Jin, H.L.; Kim, C.; Rubinstein, J.L.; Chan, W.C.W.; Cao, W.G.; Wang, L.V.; Zheng, G. Porphysome nanovesicles generated by porphyrin bilayers for use as multimodal biophotonic contrast agents. *Nat. Mater.* **2011**, *10*, 324–332. [[CrossRef](#)]
5. Chen, W.R.; Adams, R.L.; Higgins, A.K.; Bartels, K.E.; Nordquist, R.E. Photothermal effects on murine mammary tumors using indocyanine green and an 808-nm diode laser: An in vivo efficacy study. *Cancer Lett.* **1996**, *98*, 169–173. [[CrossRef](#)]
6. Yang, J.; Choi, J.; Bang, D.; Kim, E.; Lim, E.K.; Park, H.; Suh, J.S.; Lee, K.; Yoo, K.H.; Kim, E.K.; et al. Convertible organic nanoparticles for near-infrared photothermal ablation of cancer cells. *Angew. Chem. Int. Ed.* **2011**, *50*, 441–444. [[CrossRef](#)]
7. Zhang, J.Z.; Sun, D.D.; Zhang, B.; Sun, Q.Q.; Zhang, Y.; Liu, S.R.; Wang, Y.M.; Liu, C.T.; Chen, J.Z.; Chen, J.B.; et al. Intrinsic carbon nanotube liquid crystalline elastomer photoactuators for high-definition biomechanics. *Mater. Horiz.* **2022**, *9*, 1045–1056. [[CrossRef](#)]
8. Wang, Y.; Zhu, W.G.; Du, W.N.; Liu, X.F.; Zhang, X.T.; Dong, H.L.; Hu, W.P. Cocrystals strategy towards materials for near-infrared photothermal conversion and imaging. *Angew. Chem. Int. Ed.* **2018**, *57*, 3963–3967. [[CrossRef](#)]
9. Song, Q.; Jiao, Y.; Wang, Z.Q.; Zhang, X. Tuning the energy gap by supramolecular approaches: Towards near-infrared organic assemblies and materials. *Small* **2016**, *12*, 24–31. [[CrossRef](#)]
10. Qian, G.; Wang, Z.Y. Near-infrared organic compounds and emerging applications. *Chem. Asian J.* **2010**, *5*, 1006–1029. [[CrossRef](#)]
11. Li, T.T.; Dang, L.L.; Zhao, C.C.; Lv, Z.Y.; Yang, X.G.; Zhao, Y.; Zhang, S.H. A self-sensitized Co (II)-MOF for efficient visible-light-driven hydrogen evolution without additional cocatalysts. *J. Solid State Chem.* **2021**, *304*, 122609–122614. [[CrossRef](#)]
12. Qin, J.H.; Xu, P.; Huang, Y.D.; Xiao, L.Y.; Lu, W.W.; Yang, X.G.; Ma, L.F.; Zang, S.S. High loading of Mn(II)-metalated porphyrin in MOF for photocatalytic CO<sub>2</sub> reduction in gas–solid condition. *Chem. Commun.* **2021**, *57*, 8468–8471. [[CrossRef](#)]
13. Huang, Y.B.; Liang, J.; Wang, X.S.; Cao, R. Multifunctional metal-organic framework catalysts: Synergistic catalysis and tandem reactions. *Chem. Soc. Rev.* **2017**, *46*, 126–157. [[CrossRef](#)]
14. Chang, X.H.; Qin, W.J.; Zhang, X.Y.; Jin, X.; Yang, X.G.; Dou, C.X.; Ma, L.F. Angle-Dependent polarized emission and photoelectron performance of dye-encapsulated metal-organic framework. *Inorg. Chem.* **2021**, *60*, 10109–10113. [[CrossRef](#)]
15. Yang, X.G.; Zhai, Z.M.; Lu, X.M.; Qin, J.H.; Li, F.F.; Ma, L.F. Hexanuclear Zn(II)-Induced dense  $\pi$ -Stacking in a metal-organic framework featuring Long-Lasting room temperature phosphorescence. *Inorg. Chem.* **2020**, *59*, 10395–10399. [[CrossRef](#)]
16. Chang, X.H.; Ling, X.L.; Lu, X.M.; Yang, X.G.; Li, F.F.; Guo, Y.M. Near-infrared phosphorescence emission of three-fold interpenetrated MOF based on 1,4-bis(imidazole-1-ylmethyl)benzene: Syntheses, structure and photoelectron performance. *J. Solid State Chem.* **2020**, *292*, 121694. [[CrossRef](#)]
17. Zeng, L.; Guo, X.Y.; He, C.; Duan, C.Y. Metal-organic frameworks: Versatile materials for heterogeneous photocatalysis. *ACS Catal.* **2016**, *6*, 7935–7947. [[CrossRef](#)]
18. Luo, F.; Yang, C.S.; Dang, L.L.; Krishna, R.; Zhou, W.; Wu, H.; Dong, X.L.; Han, Y.; Hu, T.L.; Keeffe, M.Z.; et al. UTSA-74: A MOF-74 isomer with two accessible binding sites per metal center for highly selective gas separation. *J. Am. Chem. Soc.* **2016**, *138*, 5678–5684. [[CrossRef](#)]
19. Huang, J.; Li, Y.; Huang, R.K.; He, C.T.; Gong, L.; Hu, Q.; Wang, L.S.; Xu, Y.T.; Tian, X.Y.; Liu, S.Y.; et al. Electrochemical exfoliation of pillared-layer metal-organic framework to boost the oxygen evolution reaction. *Angew. Chem.* **2018**, *130*, 4722–4726. [[CrossRef](#)]

20. Böhme, U.; Barth, B.; Paula, C.; Kuhnt, A.; Schwieger, W.; Mundstock, A.; Caro, J.; Hartmann, M. Ethene/ethane and propene/propane separation via the olefin and paraffin selective metal–organic framework adsorbents CPO-27 and ZIF-8. *Langmuir* **2013**, *29*, 8592–8600. [[CrossRef](#)]
21. Gao, Z.; Yu, Z.W.; Liu, F.Q.; Yu, Y.; Su, X.M.; Wang, L.; Xu, Z.Z.; Yang, Y.L.; Wu, G.R.; Feng, X.F.; et al. Ultralow content iron-decorated Ni-MOF-74 fabricated by a metal-organic framework surface reaction for efficient electrocatalytic water oxidation. *Inorg. Chem.* **2019**, *58*, 11500–11507. [[CrossRef](#)]
22. Li, H.L.; Eddaoudi, M.; O’Keeffe, M.; Yaghi, O.M. Design and synthesis of an exceptionally stable and highly porous metal-organic framework. *Nature* **1999**, *402*, 276–279. [[CrossRef](#)]
23. Zhao, Y.; Wang, Y.J.; Wang, N.; Zheng, P.; Fu, H.R.; Han, M.L.; Ma, L.F.; Wang, L.Y. Tetraphenylethylene-Decorated Metal–Organic Frameworks as Energy-Transfer Platform for the Detection of Nitro-Antibiotics and White-Light Emission. *Inorg. Chem.* **2019**, *58*, 12700–12706. [[CrossRef](#)]
24. Dang, L.L.; Li, T.T.; Cui, Z.; Sui, D.; Ma, L.F.; Jin, G.X. Selective construction and stability studies of a molecular trefoil knot and Solomon link. *Dalton Trans.* **2021**, *50*, 16984–16989. [[CrossRef](#)]
25. Yang, X.G.; Liu, X.Y.; Zhai, Z.M.; Qin, J.H.; Chang, X.H.; Han, M.L.; Li, F.F.; Ma, L.F.  $\pi$ -Type halogen bonding enhanced long-last room temperature phosphorescence of Zn(II) coordination polymers for photoelectron response applications. *Inorg. Chem. Front.* **2020**, *7*, 2224–2230. [[CrossRef](#)]
26. Dang, L.L.; Li, T.T.; Zhao, C.C.; Zhang, T.T.; Ye, X.Y.; Sun, X.T.; Wang, H.R.; Ma, L.F. Supramolecular Rh6 catalytic system promoting directed [4+4] cycloaddition reaction of anthracene under UV irradiation. *J. Solid State Chem.* **2022**, *306*, 122785–122792. [[CrossRef](#)]
27. Qin, J.H.; Huang, Y.D.; Zhao, Y.; Yang, X.G.; Li, F.F.; Wang, C.; Ma, L.F. Highly dense packing of chromophoric linkers achievable in a Pyrene-Based Metal–Organic framework for photoelectric response. *Inorg. Chem.* **2019**, *58*, 15013–15016. [[CrossRef](#)]
28. Wang, H.R.; Yang, X.G.; Qin, J.H.; Ma, L.F. Long-lived room temperature phosphorescence of organic–inorganic hybrid systems. *Inorg. Chem. Front.* **2021**, *8*, 1942–1950. [[CrossRef](#)]
29. Wang, H.; Meng, W.; Wu, J.; Ding, J.; Hou, H.; Fan, Y. Crystalline central-metal transformation in metal-organic frameworks. *Coord. Chem. Rev.* **2016**, *307*, 130–146. [[CrossRef](#)]
30. Zhang, T.; Cao, J.W.; Jiang, X.; Chen, J.; Chen, T.W.; Chen, K.J. Band gap modulation enabled by TCNQ loading in a Ru-based metal–organic framework for enhanced near-infrared absorption and photothermal conversion. *Cryst. Growth Des.* **2021**, *21*, 729–734. [[CrossRef](#)]
31. Yan, T.; Li, Y.Y.; Su, J.; Wang, H.Y.; Zuo, J.L. Charge transfer metal-organic framework containing redox-active TTF/NDI units for highly efficient near-infrared photothermal conversion. *Chem. Eur. J.* **2021**, *27*, 11050–11055. [[CrossRef](#)]
32. Lü, B.Z.; Chen, Y.F.; Li, P.Y.; Wang, B.; Müllen, K.; Yin, M.Z. Stable radical anions generated from a porous perylene diimide metal-organic framework for boosting near-infrared photothermal conversion. *Nat. Commun.* **2019**, *10*, 767. [[CrossRef](#)]
33. Liu, Y.G.; Liu, G.L.; Peng, T.; Gu, C.; Gu, C.; Li, J.J.; Liu, X.Q.; Sun, L.B. Near-infrared light triggered release of ethane from a photothermal metal-organic framework. *Chem. Eng. J.* **2021**, *420*, 130490. [[CrossRef](#)]
34. Dang, L.L.; Li, T.T.; Zhang, T.T.; Zhao, Y.; Chen, T.; Gao, X.; Ma, L.F.; Jin, G.X. Highly selective synthesis and near-infrared photothermal conversion of metalla-Borromean ring and [2]catenane assemblies. *Chem. Sci.* **2022**, *13*, 5130–5140. [[CrossRef](#)]
35. Wang, Y.F.; Li, S.H.; Ma, L.F.; Geng, J.L.; Wang, L.Y. Syntheses, crystal structures, and magnetic studies of two cobalt(II) coordination polymers based on concurrent ligand extension. *Inorg. Chem. Commun.* **2015**, *62*, 42–46. [[CrossRef](#)]
36. Yan, T.; Li, Y.Y.; Gu, Q.Y.; Li, J.; Su, J.; Wang, H.Y.; Zuo, J.L. A Tetrathiafulvalene/Naphthalene Diimide-Containing Metal–Organic Framework with fsc Topology for Highly Efficient Near-Infrared Photothermal Conversion. *Inorg. Chem.* **2022**, *61*, 3078–3085. [[CrossRef](#)]
37. Wu, X.; Fu, H.; Han, M.; Zhou, L.; Ma, L. Tetraphenylethylene Immobilized Metal–Organic Frameworks: Highly Sensitive Fluorescent Sensor for the Detection of  $\text{Cr}_2\text{O}_7^{2-}$  and Nitroaromatic Explosives. *Cryst. Growth Des.* **2017**, *17*, 6041–6048. [[CrossRef](#)]
38. Chang, X.H.; Qin, J.H.; Han, M.L.; Ma, L.F.; Wang, L.Y. Exploring the structural diversities and magnetic properties of copper(II) and manganese(II) complexes based on 5-methoxyisophthalate and flexible bis(imidazole) ligands. *CrystEngComm* **2014**, *16*, 870–882. [[CrossRef](#)]
39. Zhou, Z.; Wang, Y.; Peng, F.; Meng, F.; Zha, J.J.; Ma, L.; Du, Y.H.; Peng, N.; Ma, L.F.; Zhang, Q.H.; et al. Intercalation-activated layered  $\text{MoO}_3$  nanobelts as biodegradable nanozymes for tumor-specific photo-enhanced catalytic therapy. *Angew. Chem. Int. Ed.* **2022**, *61*, e202115939.
40. Yang, X.G.; Zhai, Z.M.; Lu, X.M.; Ma, L.F.; Yan, D.P. Fast crystallization-deposition of orderly molecule level heterojunction thin films showing tunable up-conversion and ultrahigh photoelectric response. *ACS Cent. Sci.* **2020**, *6*, 1169–1178. [[CrossRef](#)]
41. Yang, X.G.; Qin, J.H.; Huang, Y.D.; Zhai, Z.M.; Ma, L.F.; Yan, D.P. Highly enhanced UV-vis-NIR light harvesting and photoelectric conversion of pyrene MOF by encapsulation of D- $\pi$ -A cyanine dye. *J. Mater. Chem. C* **2020**, *8*, 17169–17175. [[CrossRef](#)]
42. Dang, L.L.; Chen, T.; Zhang, T.T.; Li, T.T.; Song, J.L.; Zhang, K.J.; Ma, L.F. Size-Induced Highly Selective Synthesis of Organometallic Rectangular Macrocycles and Heterometallic Cage Based on Half-Sandwich Rhodium Building Block. *Molecules* **2022**, *27*, 3756. [[CrossRef](#)]
43. Xue, X.; Wang, H.; Han, Y.; Hou, H. Photoswitchable nonlinear optical properties of metal complexes. *Dalton Trans.* **2018**, *47*, 13–22. [[CrossRef](#)]

44. Qin, J.H.; Zhang, H.; Sun, P.; Huang, Y.D.; Shen, Q.; Yang, X.G.; Ma, L.F. Ionic liquid induced highly dense assembly of porphyrin in MOF nanosheets for photodynamic therapy. *Dalton Trans.* **2020**, *49*, 17772–17778. [[CrossRef](#)]
45. Gao, X.; Cui, Z.; Shen, Y.R.; Liu, D.; Lin, Y.J.; Jin, G.X. Synthesis and Near-Infrared photothermal conversion of discrete supramolecular topologies featuring Half-Sandwich [Cp\*Rh] units. *J. Am. Chem. Soc.* **2021**, *143*, 17833–17842. [[CrossRef](#)]
46. Lu, Y.; Liu, D.; Lin, Y.J.; Jin, G.X. A Hierarchical Assembly Strategy for Near-Infrared Photothermal Conversion: Unconventional Heterogeneous Metalla[2]catenanes. *Chem. Sci.* **2020**, *11*, 11509–11513. [[CrossRef](#)]
47. Zhao, Y.; Yang, X.G.; Lu, X.M.; Yang, C.D.; Fan, N.N.; Yang, Z.T.; Wang, L.Y.; Ma, L.F. {Zn<sub>6</sub>} Cluster Based Metal–Organic Framework with Enhanced Room-Temperature Phosphorescence and Optoelectronic Performances. *Inorg. Chem.* **2019**, *58*, 6215–6221. [[CrossRef](#)]
48. Zhang, T.T.; Chen, T.; Dang, L.L.; Li, T.T.; Sun, K.X.; Gao, Y.J.; Ma, L.F.; Li, D.S. Self-assembly and near-infrared photothermal conversion research of molecular figure-of-eight. *J. Solid State Chem.* **2022**, *313*, 123320–123328. [[CrossRef](#)]
49. Dang, L.L.; Zhang, T.T.; Li, T.T.; Chen, T.; Zhao, Y.; Zhao, C.C.; Ma, L.F. Stable Zinc-Based Metal-Organic Framework Photocatalyst for Effective Visible-Light-Driven Hydrogen Production. *Molecules* **2022**, *27*, 1917. [[CrossRef](#)]
50. Sheldrick, G.M. A short history of SHELX. *Acta Crystallogr.* **2008**, *A64*, 112–122. [[CrossRef](#)]
51. Sheldrick, G.M. Phase annealing in SHELX-90: Direct methods for larger structures. *Acta Crystallogr. Sect. A Found. Crystallogr.* **1990**, *46*, 467–473. [[CrossRef](#)]